Available online at www.sciencedirect.com
ScienceDirect
Journal of the European Ceramic Society 28 (2008) 3071–3081
www.elsevier.com/locate/jeurceramsoc

Yb_2O_3 and Gd_2O_3 doped strontium zirconate for thermal barrier coatings

W. Ma [a,*], D. Mack [a], J. Malzbender [b], R. Vaßen [a], D. Stöver [a]

[a] *Institut für Energieforschung 1 (IEF-1), Forschungszentrum Jülich GmbH, D-52425 Jülich, Germany*
[b] *Institut für Energieforschung 2 (IEF-2), Forschungszentrum Jülich GmbH, D-52425 Jülich, Germany*

Received 22 December 2007; received in revised form 4 May 2008; accepted 9 May 2008
Available online 30 June 2008

Abstract

Yb_2O_3 (10 mol%) and Gd_2O_3 (20 mol%) doped $SrZrO_3$ was investigated as a material for thermal barrier coating (TBC) applications. The thermal expansion coefficients (TECs) of sintered bulk $Sr(Zr_{0.9}Yb_{0.1})O_{2.95}$ and $Sr(Zr_{0.8}Gd_{0.2})O_{2.9}$ were recorded by a high-temperature dilatometer and revealed a positive influence on phase transformations of $SrZrO_3$ by doping Yb_2O_3 or Gd_2O_3. The results for the thermal conductivities of $Sr(Zr_{0.9}Yb_{0.1})O_{2.95}$ and $Sr(Zr_{0.8}Gd_{0.2})O_{2.9}$ indicated that both dopants can reduce the thermal conductivity of $SrZrO_3$. Mechanical properties (Young's modulus, hardness, and fracture toughness) of dense $Sr(Zr_{0.9}Yb_{0.1})O_{2.95}$ and $Sr(Zr_{0.8}Gd_{0.2})O_{2.9}$ showed lower Young's modulus, hardness and comparable fracture toughness with respect to YSZ. The cycling lifetimes of $Sr(Zr_{0.9}Yb_{0.1})O_{2.95}$/YSZ and $Sr(Zr_{0.8}Gd_{0.2})O_{2.9}$/YSZ double layer coatings (DLC), which were prepared by plasma spraying, were comparable to that of YSZ at operating temperatures <1300 °C. However, the cycling lifetime of $Sr(Zr_{0.9}Yb_{0.1})O_{2.95}$/YSZ DLC was ~25% longer, whereas $Sr(Zr_{0.8}Gd_{0.2})O_{2.9}$/YSZ DLC had a shorter lifetime compared to the optimized YSZ coating at operating temperatures >1300 °C.

Keywords: Thermal barrier coatings; Perovskites; Thermal properties; Lifetime; $SrZrO_3$

1. Introduction

In the last two decades, more and more efforts have been devoted to the development and manufacture of ceramic TBCs in gas turbines.[1] State-of-the-art TBCs are based on 7–8 wt% Y_2O_3-stabilized ZrO_2 (YSZ), deposited by atmospheric plasma spraying (APS) or electron-beam physical vapor deposition (EB-PVD).[2] The maximum surface temperature of YSZ is limited to ~1200 °C for long-term operation. At higher temperatures, phase transformations occur from the t′-tetragonal to tetragonal and cubic (t + c) and then to monoclinic (m) zirconia, giving rise to a volume change and possibly resulting in the formation of cracks in the coatings.[3]

Therefore, new TBC materials are under investigation to further increase the inlet temperature of the turbine engines with a consequent improvement in efficiency. Several types of oxides considered as TBC candidate materials are below[4]:

fluorite structure oxides such as YSZ–Nd (Gd, Sm)–Yb,[5] HfO_2–Y_2O_3,[6] $La_2Ce_2O_7$[7,8]; pyrochlore structure oxides such as zirconates of Gd, Eu, Sm, Nd, and La[9–12]; other oxides such as $Y_3Al_xFe_{5-x}O_{12}$,[13] $LaPO_4$,[14] and $LaMgAl_{11}O_{19}$.[15]

In contrast to these other classes of oxides, perovskites (ABO_3) are characterized by high melting points, low thermal conductivities and high TECs. Perovskites additionally offer the possibility of extensive substitution of ions at the A and B sites, which enable the properties of the materials to be selectively influenced by mixed-crystal formation.[16] Two perovskite materials, $BaZrO_3$ and $SrZrO_3$, were evaluated as TBC candidate materials. $BaZrO_3$ showed relatively poor thermal chemical stability with a consequence of early failure in thermal cycling tests, while $SrZrO_3$ was not evaluated as a coating due to its phase transformations at high temperatures.[17]

The ideal perovskite ABO_3 is cubic symmetry, in space group $Pm\bar{3}m$. The structure is commonly visualized as a three-dimensional network of regular corner-linked BX_6 octahedra, the B cations being at the center of these octahedra and the A cations being centrally located in the spaces between them. The most commonly occurring distortion in perovskites is octahedral tilting. This means that the tilting of the BX_6 octahedra about one or more of their symmetry axes, maintaining both regularity of the octahedral (approximately) and their corner connectivity

* Corresponding author. Tel.: +49 2461 612877; fax: +49 2461 612455.
E-mail address: wma66@163.com (W. Ma).

0955-2219/$ – see front matter © 2008 Elsevier Ltd. All rights reserved.
doi:10.1016/j.jeurceramsoc.2008.05.013

(strictly). Such tilting allows greater flexibility in the coordination of the A cation, while leaving the environment of the B cation essentially unchanged. It is also a major contributor to structural variability in perovskites.[18] $SrZrO_3$ is a perovskite showing three temperature-induced phase transformations, but octahedral tilting is considered to be the only distorting involved. Carlsson (1967) was the first to examine these phase transformations, using both X-ray and thermal analysis methods.[19] He summarized his observations in the schematic:

$$\text{orthorhombic} \xrightarrow{700^\circ\text{C}} \text{pseudo-tetragonal} \xrightarrow{830^\circ\text{C}} \text{tetragonal} \xrightarrow{1130^\circ\text{C}} \text{cubic}$$

Ahtee et al. (1976, 1978) used neutron powder diffraction to establish the room temperature orthorhombic structure as that in *Pnma* and recorded two diffraction patterns at elevated temperatures in an effort to establish the structures of the higher-temperature forms.[20,21] They found the tetragonal phase (at 900 °C) to be that in *I*4/*mcm* while the orthorhombic phase (at 760 °C) in *Bmmb*. Howard et al. (2000) re-examined the phase transformations in $SrZrO_3$ using very high resolution neutron powder diffraction, and working at a small rate of temperature increase from room temperature to 1230 °C.[22] The structure was confirmed by the Rietveld method and summarized as

$$\underset{Pnma}{\text{orthorhombic}} \xrightarrow{750^\circ\text{C}} \underset{Imma}{\text{pseudo-tetragonal}} \xrightarrow{840^\circ\text{C}} \underset{I4/\text{mcm}}{\text{tetragonal}} \xrightarrow{1130^\circ\text{C}} \underset{Pm\bar{3}m}{\text{cubic}},$$

a sequence entirely consistent with Carlsson's observations.

As a TBC candidate material, the phase transformations for $SrZrO_3$ from room temperature to high temperatures are not desired. However, they are transformed into each other with a small volume change. Zhao et al. (1991) used high-temperature X-ray diffraction to study the thermal expansion of $SrZrO_3$, and suggested that both the transformations of *Pnma–Imma* and *Imma–I*4/*mcm* in $SrZrO_3$ are first order phase transformations. However, there are no distinguishable discontinuities in unit cell volumes for any of the structural phase transformations of $SrZrO_3$. These phase transformations are thus considered to be nearly continuous and very close to the second order phase transformation.[23] Ligny et al. (1996) used energy-dispersive X-ray diffraction to study the thermal expansion of $SrZrO_3$, and only the phase transformation from orthorhombic *Pnma* to pseudo-tetragonal *Imma* at 700 °C was detected with a small volume change of 0.14%.[24]

In the present paper, the rare earth oxides Yb_2O_3 and Gd_2O_3 were selected as two dopants in an attempt to improve phase stability and TEC of $SrZrO_3$, as well as to decrease its thermal conductivity. The Yb_2O_3 and Gd_2O_3 doped $SrZrO_3$ coatings, as well as their DLC (inner layer was YSZ), were prepared by APS and their thermal cycling lifetime was evaluated using a burner rig test.

2. Low thermal conductivity criteria and formability of ABO_3 perovskite

2.1. Low thermal conductivity criteria

In electronic insulator crystalline solids, heat is transferred by lattice vibrations and radiation. For zirconia, phonon transport dominates the heat conduction below 1200 °C, while radiation becomes more significant with further temperature increase (a contribution of approximately 10% at 1250 °C).[25] Therefore, this is expected to be a significant factor in the performance of high-powered, high-efficiency engines. Radiation is not discussed in the present paper, because it occurs at high temperatures.

In the case where lattice vibrations dominate heat transfer, the thermal conductivity can be calculated using[26]

$$\lambda = \frac{1}{3}\int C(\omega)\nu l(\omega)\mathrm{d}\omega \tag{1}$$

where C is the specific heat capacity of the material, ν is the phonon velocity, l is the phonon mean free path, and ω is the phonon frequency.

To lower the intrinsic thermal conductivity of a material, reductions in the specific heat capacity, phonon velocity, phonon mean free path are needed. The specific heat capacity at constant volume for any system is constant at a value of $\sim$25 J K^{-1} mol^{-1} when above the Debye temperature.[27] The phonon velocity can be approximated by[28]

$$\nu = A\sqrt{\frac{E}{\rho}} \tag{2}$$

where A has a value of 0.87 ± 0.02, E is Young's modulus, ρ is the density. The phonon mean free path can be approximately described by[29]

$$\frac{1}{l} = \frac{1}{l_\mathrm{i}} + \frac{1}{l_\mathrm{p}} + \frac{1}{l_\mathrm{b}} \tag{3}$$

where l_i, l_p, and l_b are the phonon mean free paths due to intrinsic conductivity, point defect scattering, and grain-boundary scattering, respectively. Of these the grain-boundary scattering has the least effect on the phonon mean free path in conventional materials, but may provide a significant effect in nanostructured coatings.[30] Therefore, the phonon mean free path is affected strongly by point defect scattering. The most important point defects are vacancies. The introduction of vacancies and local strain fields, especially generated by incorporating large dopant atoms with lower valence, can reduce the phonon mean free path. These vacancies and strain fields act to scatter phonons thus directly increasing phonon scattering in the lattice. With increased phonon scattering, there is a high probability that phonon–phonon interactions will occur further reducing the phonon mean free path. At high temperatures, the thermal conductivity approaches a minimum value and can be expressed by[28]

$$\lambda_\mathrm{min} = 0.87 k_B \bar{\Omega}_\mathrm{a}^{-2/3}\left(\frac{E}{\rho}\right)^{1/2} \tag{4}$$

where $\bar{\Omega}_\mathrm{a}$ is an effective atomic volume

$$\bar{\Omega}_\mathrm{a} = \frac{M}{m\rho N_A} \tag{5}$$

Table 1
Covalent radii, tolerant factor and octahedral factor of studied perovskite

Perovskite	r_A (CN = 12)	r_B (CN = 6)	Tolerant factor, t	Octahedral factor, r_B/r_O
$SrZrO_3$	1.44	0.72	0.95	0.51
Zr^{4+} replaced by Yb^{3+}	1.44	0.86	0.89	0.61
Zr^{4+} replaced by Gd^{3+}	1.44	0.94	0.86	0.66

where M is the mean atomic mass of the ions in the unit cell, m is the number of ions in the unit cell, k_B and N_A are Boltzmann's constant and Avagadro's number, respectively.

These expressions indicate that a large mean atomic mass and a low Young's modulus favor low thermal conductivity. An additional concept is to introduce randomly distributed point defects into a structure at a sufficiently high density so they will cause inelastic phonon scattering with the consequence of decreasing the phonon mean free path as well as the attainable thermal conductivity.

2.2. Formability of ABO_3 perovskite

It is well known that Goldschmidt's "tolerance factor" ($t = r_A + r_O/\sqrt{2}(r_B + r_O)$, where r_A, r_B and r_O are the ionic radii of A, B and O, respectively) is used to study the stability of perovskites. The tolerance factor t has been widely accepted as a criterion for the formation of the perovskite structure, and up to now almost all known perovskite compounds have t values in the range of 0.75–1.00. However, it seems that $t = 0.75$–1.00 is not a sufficient condition for the formation of the perovskite structure, as indicated for some systems (Cu_2O–P_2O_5, Li_2O–As_2O_3, MnO–GeO_2, Al_2O_3–B_2O_3), whose t is even within the most favorable range (0.8–0.9), but where there is no stable perovskite structure.[31] Therefore, additional parameters may be necessary for the prediction of perovskite formation. It is well known that the octahedron BO_6 is the basic structure unit for perovskite structure, thus the ratio of the ionic radius (r_B/r_O) (denoted as the octahedral factor) is proposed as another formation indicator of perovskite structure.[32] The lowest limit of the octahedral factor for perovskite formation is 0.425.[31]

The tolerance factor t and octahedral factor of Yb_2O_3 and Gd_2O_3 doped $SrZrO_3$ are listed in Table 1. The ionic radii used here are taken from the literature.[33]

3. Experimental procedure

Yb_2O_3 (10 mol%) and Gd_2O_3 (20 mol%) doped $SrZrO_3$ (denoted as modified $SrZrO_3$) powders were synthesized using $SrCO_3$ (Aldrich, >98%), ZrO_2 (Aldrich, 99%), Yb_2O_3 (Treibacher Powdermet, 99.9%) and Gd_2O_3 (Treibacher Powdermet, 99.9%) powders by a solid-state reaction. The starting materials were ball-milled and, after drying, calcined at 1400 °C and ball-milled again. The treatment was repeated three times in an attempt to obtain a single-phase material. The phase analysis of the synthesized powders was characterized by XRD (Model D5000, Siemens, Cu K_α radiation, Germany).

The modified $SrZrO_3$ bulk materials were sintered at 1600 °C for 6 h in air. The thermal expansion coefficients, thermal diffusivities and specific heat capacities of the modified $SrZrO_3$ bulk materials were recorded by a high-temperature dilatometer (Model DIL 402E, Netzsch, Germany), the laser flash method (Model THETA, Netzsch, Germany) and simultaneous thermal analysis apparatus (Model STA 449C, Netzsch, Germany), respectively. The densities (ρ) of the sintered samples were measured according to the Archimedes' principle. The thermal conductivities of the sintered samples were calculated using the equation:

$$\lambda = D_{th}(T)C_p(T)\rho(T) \quad (6)$$

where λ, $D_{th}(T)$, $C_p(T)$, and $\rho(T)$ are the thermal conductivity, thermal diffusivity, specific heat capacity, and measured density, respectively.

For measurements of the mechanical properties the samples were prepared by cold pressing, which was followed by hot-pressing sintering at 1550 °C at 100 MPa for 2–4 h. The disc-shaped samples thus prepared were cold mounted using resin and polished to less than 1 μm. Young's modulus and hardness of the modified $SrZrO_3$ were determined by a depth-sensing microindentation technique, in which the indenter position was precisely recorded at a given applied load. The instrument (Model H–100 Fischerscope, Helmut Fischer GmbH, Germany) displays the indenter displacement with an accuracy in the nanometer range and a load resolution of 0.4 mN during the entire loading–unloading period. A fracture toughness of the modified $SrZrO_3$ was determined using a conventional hardness tester with applied loads of 2, 3, and 5 N.

For plasma spraying, the modified $SrZrO_3$ powders synthesized by a solid-state reaction were milled with ethanol and 1.8 wt% dispersing agent, and subsequently spray-dried. Sieved size fractions between 45 and 125 μm were used for plasma spraying. The YSZ powder used was a 7.8 wt% yttria-stabilized zirconia powder (Metco 204 NS, Sulzer Metco GmbH, Germany).

The modified $SrZrO_3$ coating and the modified $SrZrO_3$/YSZ DLC were air plasma sprayed (Triplex I gun, Sulzer Metco, Switzerland) on the different substrates (IN738 and steel) with a total coating thickness of about 400 μm. The deposition conditions for the coatings were argon and helium plasma gas flow rates of 20 and 13 standard liter per minute (slpm), a plasma current of 300 A at a power of 20 kW, and a spray distance of 100 mm. The DLC consisted of an YSZ coating directly deposited on the bondcoat and a modified $SrZrO_3$ topcoat. The thickness of each coating was about half the total coating thickness.

For thermal cycling, the coatings were sprayed on an IN738 substrate which had a diameter of 30 mm and a thickness of 3 mm. The disc-shaped samples had a beveled edge to minimize

Table 2
Results of thermal cycling tests of the modified $SrZrO_3$ coatings and the modified $SrZrO_3$/YSZ DLC

Sample	TBC system	$T_{surface}$ (°C)	$T_{substrate}$ (°C)	Cycles to failure	TGO thickness (μm)
WDS927	$SrZrO_3$	1251	965	1514	8.8/7.6/7.6
WDS1001	$Sr(Zr_{0.8}Gd_{0.2})O_{2.9}$	1130	984	13	–/–/–
WDS1002	$Sr(Zr_{0.8}Gd_{0.2})O_{2.9}$/YSZ	1249	965	3853	7.2/8.4/8.2
WDS1003		1348	1015	208	3.0/5.8/5.0
WDS1004	$Sr(Zr_{0.9}Yb_{0.1})O_{2.95}$/YSZ	1246	974	3443	9.2/8.8/–
WDS1005		1329	1011	1285	6.6/6.2/–
WDS1006	$Sr(Zr_{0.9}Yb_{0.1})O_{2.95}$	1239	969	806	6.0/7.6/7.8
–	Typical YSZ[34]	1320–1350	1000–1035	250–1000	–/–/–

For comparison also typical YSZ TBCs are given. The thickness of thermally grown oxide (TGO) is given at three locations: first upper left rim, then middle, and finally lower right rim for the photos shown in Fig. 6(b), 7(a), 8(a) and 9(a).

the effect of stresses originating at the free edges of the samples. Before deposition of the final topcoat, the substrates were coated with a 150 μm Ni–Co–Cr–Al–Y bondcoat by vacuum plasma spraying (VPS) in a Sulzer Metco facility using an F4 gun. Steel substrates were also coated during fabrication of the thermal cycling specimens. These coatings were used to characterize the as-sprayed condition. The freestanding coatings, which were produced by removing the steel substrate from the coating with hydrochloric acid, were used to investigate the pore-size distribution (Models Pascal 140 and 440, CE Instruments, Italy).

Thermal cycling was performed on the disc-shaped samples in a gas-burner test facility operated with natural gas and oxygen. The substrate was cooled from the back by compressed air. The surface temperature was measured using a pyrometer operated at a wavelength of 8–13 μm. Emissivity was determined for conventional YSZ TBC as ~1. This value was also taken for the above-mentioned coatings, which might lead to an underestimation of the surface temperature. A 1 mm hole was radially drilled half-way through the thickness of the substrate to the center of the disc. A thermocouple was introduced to measure the substrate temperature at this location. The maximum temperature was reached after heating for ~20 s. After 5 min heating, the burner was automatically removed from the surface for 2 min, and the surface was cooled at ~100 K/s using compressed air. Cycling was stopped when a clearly visible spallation (about 5 mm × 5 mm at least) of the coating occurred at the central part. The results of thermal cycling tests of the modified $SrZrO_3$ coatings and the modified $SrZrO_3$/YSZ DLC are listed in Table 2.

The microstructure and composition of the coatings were investigated by a scanning electron microscope (SEM) (Model JXA 840, JEOL, Japan) with an energy-dispersive X-ray spectrometer (EDX) (Model Inca, Oxford Instruments, UK).

4. Results and discussion

4.1. Thermophysical properties of the modified $SrZrO_3$ powders, their bulk materials and coatings

The relative densities of $SrZrO_3$, $Sr(Zr_{0.9}Yb_{0.1})O_{2.95}$ and $Sr(Zr_{0.8}Gd_{0.2})O_{2.9}$, which were hot-pressing sintered at 1550 °C at 100 MPa, are >95% of the theoretical densities. Moreover, the relative densities of the modified $SrZrO_3$ are slightly higher than that of $SrZrO_3$, indicating that doping Yb_2O_3 and Gd_2O_3 encourages the densification of $SrZrO_3$. These samples are used for further characterization of the physical properties.

The TECs of dense $SrZrO_3$, $Sr(Zr_{0.9}Yb_{0.1})O_{2.95}$ and $Sr(Zr_{0.8}Gd_{0.2})O_{2.9}$ are shown in Fig. 1. The TEC of $SrZrO_3$ is 8.7–10.8 × 10^{-6} K^{-1} (200–1100 °C), which is comparable to that of YSZ (~10.5 × 10^{-6} K^{-1}, 200–1100 °C).[35] The TEC of $SrZrO_3$ has an abnormal change at ~750 °C, which is in accordance with a phase transformation from orthorhombic to pseudo-tetragonal. The TEC of $Sr(Zr_{0.9}Yb_{0.1})O_{2.95}$ is 9.2–10.6 × 10^{-6} K^{-1} (200–1100 °C). Its TEC is higher below ~740 °C and comparable to that of $SrZrO_3$ between 740–1100 °C. The abnormal change in TEC occurs at ~630 °C, which is much lower than that of $SrZrO_3$, indicating that doping Yb_2O_3 can shift the phase transformation temperature to a lower temperature. With respect to $Sr(Zr_{0.8}Gd_{0.2})O_{2.9}$, its TEC is 8.4–10.5 × 10^{-6} K^{-1} (200–1100 °C), which is lower than that of $SrZrO_3$ in the whole tested temperature range. Lower TEC may lead to higher stress generation during thermal cycling, which is a disadvantage for TBC application. However, the TEC of $Sr(Zr_{0.8}Gd_{0.2})O_{2.9}$ has no obvious abnormal change during measuring, indicating that doping Gd_2O_3 can greatly improve

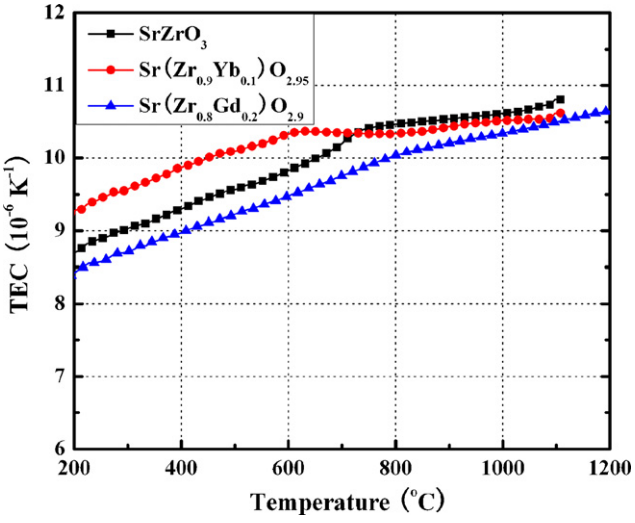

Fig. 1. TECs of $SrZrO_3$, $Sr(Zr_{0.9}Yb_{0.1})O_{2.95}$ and $Sr(Zr_{0.8}Gd_{0.2})O_{2.9}$ bulk materials sintered at 1600 °C for 6 h.

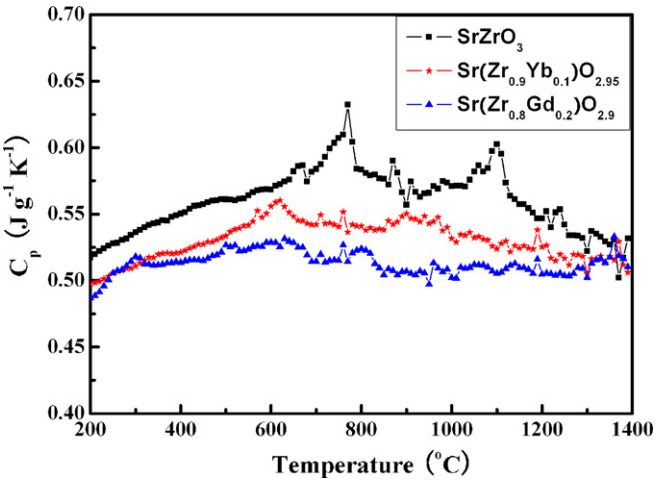

Fig. 2. Specific heat capacities of $SrZrO_3$, $Sr(Zr_{0.9}Yb_{0.1})O_{2.95}$ and $Sr(Zr_{0.8}Gd_{0.2})O_{2.9}$.

the phase stability of $SrZrO_3$. This might be due to a larger octahedral factor of r_{Gd}/r_O compared to r_{Yb}/r_O.

Fig. 2 shows the specific heat capacities (C_p) of $SrZrO_3$, $Sr(Zr_{0.9}Yb_{0.1})O_{2.95}$ and $Sr(Zr_{0.8}Gd_{0.2})O_{2.9}$. $Sr(Zr_{0.8}Gd_{0.2})O_{2.9}$ has the lowest C_p, followed by $Sr(Zr_{0.9}Yb_{0.1})O_{2.95}$ and $SrZrO_3$. Doping Yb_2O_3 and Gd_2O_3 not only suppresses the phase transformations in $SrZrO_3$, but also lowers its C_p. This yields a lower thermal conductivity (λ) for a given thermal diffusivity (D_{th}).

The thermal conductivities of $SrZrO_3$, $Sr(Zr_{0.9}Yb_{0.1})O_{2.95}$ and $Sr(Zr_{0.8}Gd_{0.2})O_{2.9}$ as a function of temperature are shown in Fig. 3. The thermal conductivity of these materials decreases with increasing temperature up to a moderate temperature, and then increases with a further temperature increase. The thermal conductivity of $Sr(Zr_{0.9}Yb_{0.1})O_{2.95}$ is not only at least ~20% lower than that of $SrZrO_3$ in the whole tested temperature range, but also ~20% lower than that of YSZ at 1000 °C (2.1–2.2 W m^{-1} K^{-1}, 1000 °C).[36] The thermal conductivity of $Sr(Zr_{0.8}Gd_{0.2})O_{2.9}$ is lower below ~900 °C and comparable between 900 and 1100 °C than that of $SrZrO_3$. The results reveal

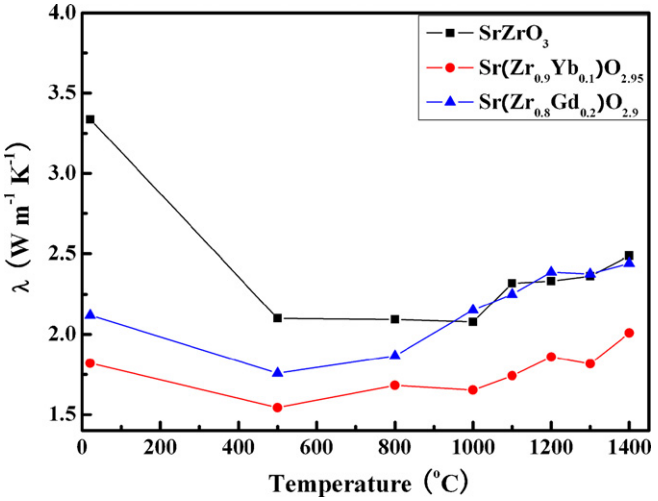

Fig. 3. Thermal conductivities of $SrZrO_3$, $Sr(Zr_{0.9}Yb_{0.1})O_{2.95}$ and $Sr(Zr_{0.8}Gd_{0.2})O_{2.9}$ as a function of temperature.

that doping Yb_2O_3 is more effective in reducing thermal conductivity for $SrZrO_3$ than doping Gd_2O_3.

It is uncertain whether the increasing values of the thermal conductivity shown at high temperatures above 1000 °C in Fig. 3 are realistic. This increase is probably caused by the method for thermal diffusivity measurement, which is the laser flash experiment. It is necessary to coat an opaque layer on the surface

Table 3
Mechanical properties of $SrZrO_3$, $Sr(Zr_{0.9}Yb_{0.1})O_{2.95}$, and $Sr(Zr_{0.8}Gd_{0.2})O_{2.9}$

Material	Young's modulus (GPa)	Hardness (GPa)	Fracture toughness (MPa m$^{1/2}$)
$SrZrO_3$	170 ± 4	9.2 ± 0.1	1.5 ± 0.1
$Sr(Zr_{0.9}Yb_{0.1})O_{2.95}$	150 ± 5	9.2 ± 0.9	1.1 ± 0.1
$Sr(Zr_{0.8}Gd_{0.2})O_{2.9}$	160 ± 5	9.2 ± 0.3	1.6 ± 0.1
YSZ[17]	210 ± 10	13 ± 1	1–2

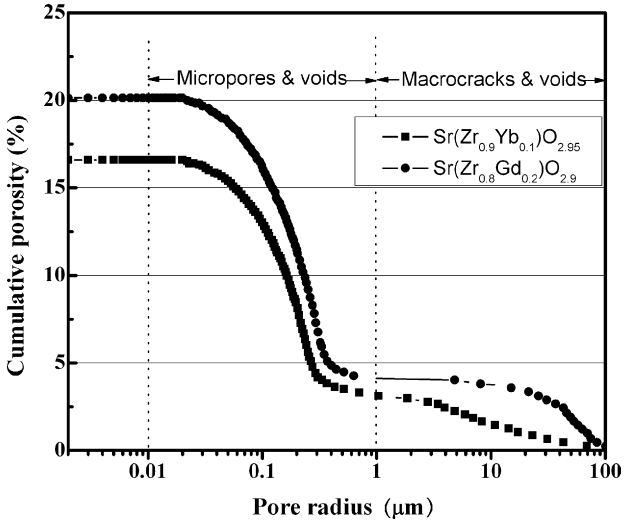

Fig. 4. Porosity distribution of $Sr(Zr_{0.9}Yb_{0.1})O_{2.95}$ and $Sr(Zr_{0.8}Gd_{0.2})O_{2.9}$ free-standing coatings in the as-sprayed case.

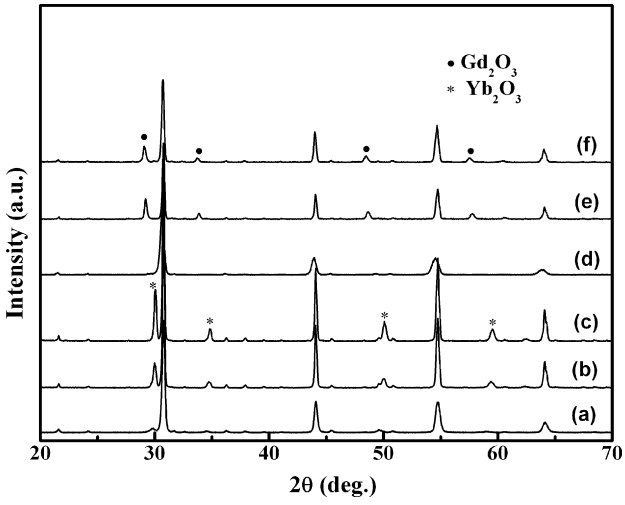

Fig. 5. Surface XRD patterns of $Sr(Zr_{0.9}Yb_{0.1})O_{2.95}$/YSZ coating as-sprayed (a), after cycling at surface temperatures of 1246 °C (b) and 1329 °C (c), of $Sr(Zr_{0.8}Gd_{0.2})O_{2.9}$/YSZ coating as-sprayed (d), after cycling at surface temperatures of 1249 °C (e) and 1348 °C (f).

of the samples for tests in the temperature region above 1000 °C, because ceramic materials are transparent for thermal radiation to a certain extent in this temperature region. The opaque layer, which was graphite in our case, tends to disintegrate at elevated temperatures. This can lead to incorrect values of the thermal diffusivity, and the value at high temperatures could therefore be too high.

Young's modulus of the modified $SrZrO_3$ was measured by an indentation technique, and the results of $SrZrO_3$ and YSZ are also presented for comparison. The mean values of the Young's modulus, the hardness and fracture toughness for these materials are given in Table 3. The Young's modulus and hardness of the modified $SrZrO_3$ are more than ∼23% and ∼29% below the values found for dense YSZ. The Young's modulus of the modified $SrZrO_3$ is also lower than that of $SrZrO_3$. A low elastic modulus value is advantageous with respect to thermal stresses. The fracture toughness of the modified $SrZrO_3$ is between 1.0 and 2.0 MPa $m^{1/2}$, which is comparable to that of YSZ and $SrZrO_3$.

Plasma-sprayed coatings of $Sr(Zr_{0.9}Yb_{0.1})O_{2.95}$ and $Sr(Zr_{0.8}Gd_{0.2})O_{2.9}$ were first optimized mainly with respect to homogeneity of the microstructure. The porosity distribution of

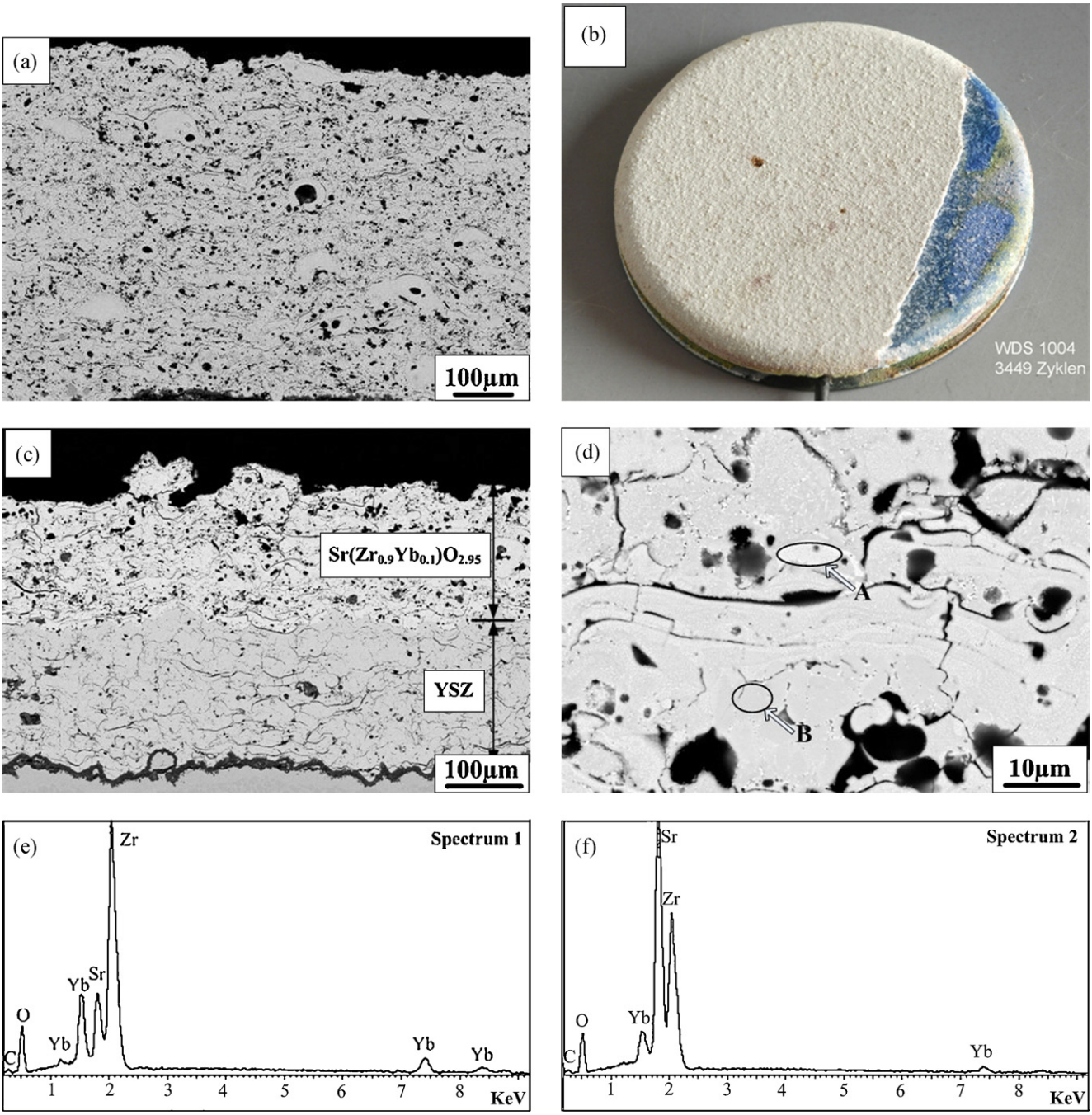

Fig. 6. Cross-section micrograph of $Sr(Zr_{0.9}Yb_{0.1})O_{2.95}$ coating as-sprayed (a), surface morphology of $Sr(Zr_{0.9}Yb_{0.1})O_{2.95}$/YSZ DLC (b), its cross-section micrographs (c) and (d), EDX spectra of areas A (e) and B (f) in (d), after cycling at a surface temperature of 1246 °C.

the modified $SrZrO_3$ coatings used for thermal cycling is shown in Fig. 4. The results reveal a typical bimodal pore size distribution. The larger defects corresponding to radii above 1 μm are believed to have resulted from macrocracks and voids. The fine pores smaller than 1 μm are mainly attributed to microcracks such as intersplat gaps and intrasplat cracks. The cumulative porosities of $Sr(Zr_{0.9}Yb_{0.1})O_{2.95}$ and $Sr(Zr_{0.8}Gd_{0.2})O_{2.9}$ free-standing coatings are ~20.0% and ~16.5%, respectively, which are slightly larger than the optimized porosity level (~15%) normally used in conventional YSZ-based TBCs.[37]

4.2. Thermal cycling behavior of $Sr(Zr_{0.9}Yb_{0.1})O_{2.95}$/YSZ and $Sr(Zr_{0.8}Gd_{0.2})O_{2.9}$/YSZ DLC

The thermal cycling results of $Sr(Zr_{0.9}Yb_{0.1})O_{2.95}$/YSZ and $Sr(Zr_{0.8}Gd_{0.2})O_{2.9}$/YSZ DLC are listed in Table 2. $Sr(Zr_{0.9}Yb_{0.1})O_{2.95}$, $Sr(Zr_{0.8}Gd_{0.2})O_{2.9}$, $SrZrO_3$ and typical YSZ coatings are also presented for comparison. It is obvious that $Sr(Zr_{0.9}Yb_{0.1})O_{2.95}$ and $Sr(Zr_{0.8}Gd_{0.2})O_{2.9}$ coatings have a short thermal cycling lifetime compared with YSZ coating. However, the thermal cycling lifetimes of $Sr(Zr_{0.9}Yb_{0.1})O_{2.95}$/YSZ and $Sr(Zr_{0.8}Gd_{0.2})O_{2.9}$/YSZ DLC at a surface temperature of ~1250 °C are 3443 cycles and 3853 cycles, respectively, which are comparable to that of YSZ and much longer than that of $SrZrO_3$. At surface temperature >1300 °C, the thermal cycling lifetime of $Sr(Zr_{0.9}Yb_{0.1})O_{2.95}$/YSZ is 1285 cycles, which is ~25% longer, whereas the thermal cycling lifetime of $Sr(Zr_{0.8}Gd_{0.2})O_{2.9}$/YSZ is much shorter than that of YSZ. The short lifetime for $Sr(Zr_{0.9}Yb_{0.1})O_{2.95}$ and $Sr(Zr_{0.8}Gd_{0.2})O_{2.9}$ coatings might be mainly due to the lower critical energy release rate compared to YSZ, since the lower critical energy release rate has a higher potential for bondcoat-ceramic delamination.[38]

The surface XRD patterns of $Sr(Zr_{0.9}Yb_{0.1})O_{2.95}$/YSZ and $Sr(Zr_{0.8}Gd_{0.2})O_{2.9}$/YSZ DLC as-sprayed and after cycling at different surface temperatures are shown in Fig. 5. The DLC have single phase in the as-sprayed case. However, after thermal cycling at high surface temperatures (~1250 or ~1350 °C) the second phase is developed, which is Yb_2O_3 for $Sr(Zr_{0.9}Yb_{0.1})O_{2.95}$/YSZ and Gd_2O_3 for $Sr(Zr_{0.8}Gd_{0.2})O_{2.9}$/YSZ. The precipitation of the second phase in the coatings is detrimental for TBC applications.

The cross-section of $Sr(Zr_{0.9}Yb_{0.1})O_{2.95}$ coating as-sprayed, morphology of $Sr(Zr_{0.9}Yb_{0.1})O_{2.95}$/YSZ coating surface and its cross-section after cycling at a surface temperature of 1246 °C are shown in Fig. 6. The EDX analysis of different areas in the $Sr(Zr_{0.9}Yb_{0.1})O_{2.95}$ layer after cycling is also presented in Fig. 6(e) and (f). As-sprayed $Sr(Zr_{0.9}Yb_{0.1})O_{2.95}$ coating is more porous compared with YSZ coating, and also has some large pores, which are caused by improper melting of large particles during spraying. $Sr(Zr_{0.9}Yb_{0.1})O_{2.95}$/YSZ coating spalled from the bondcoat (Fig. 6(b)), whereas the $Sr(Zr_{0.9}Yb_{0.1})O_{2.95}$ and YSZ layers were still intact (Fig. 6(c)). In the $Sr(Zr_{0.9}Yb_{0.1})O_{2.95}$ layer, area A is rich in the Yb element compared to area B as shown by EDX analysis, indicating that Yb precipitated upon cycling. According to the XRD results the precipitated particles are Yb_2O_3. However, the failure mechanism of the $Sr(Zr_{0.9}Yb_{0.1})O_{2.95}$/YSZ coating does not seem to be due to the precipitation of Yb_2O_3, but is similar to YSZ. The cracks develop close to the topcoat–bondcoat interface.[39] Crack propagation is driven in this case by stresses, which develop due to the mismatch in TEC upon cooling and are further enhanced by TGO growth on the bondcoat.

The morphology of the $Sr(Zr_{0.9}Yb_{0.1})O_{2.95}$/YSZ coating surface and its cross-section after cycling at a surface temperature of 1329 °C are shown in Fig. 7. The $Sr(Zr_{0.9}Yb_{0.1})O_{2.95}$/YSZ coating spalled from the bondcoat (Fig. 7(a)) and some vertical cracks are observed in the $Sr(Zr_{0.9}Yb_{0.1})O_{2.95}$ layer of the cross-section (Fig. 7(b)). The development of vertical cracks might be due to the sintering of the coating surface, which is also observed in YSZ coatings after cycling in the surface temperature range between 1320 and 1350 °C.[34]

The morphology of $Sr(Zr_{0.8}Gd_{0.2})O_{2.9}$/YSZ coating surface and its cross-section after cycling at a surface temperature of 1249 °C are shown in Fig. 8. The EDX analysis of different areas in $Sr(Zr_{0.8}Gd_{0.2})O_{2.9}$ layer is also presented in Fig. 8(e) and (f). The $Sr(Zr_{0.9}Yb_{0.1})O_{2.95}$/YSZ coating spalled from the bondcoat (Fig. 8(a)). The parallel cracks are observed

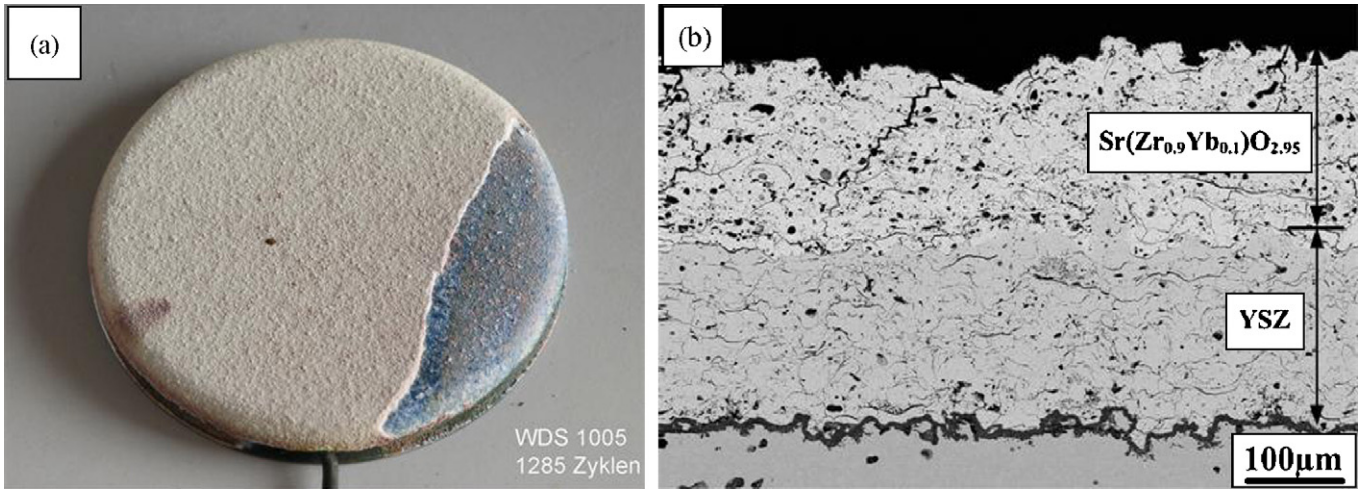

Fig. 7. Surface morphology of $Sr(Zr_{0.9}Yb_{0.1})O_{2.95}$/YSZ DLC (a) and its cross-section micrograph (b) after cycling at a surface temperature of 1329 °C.

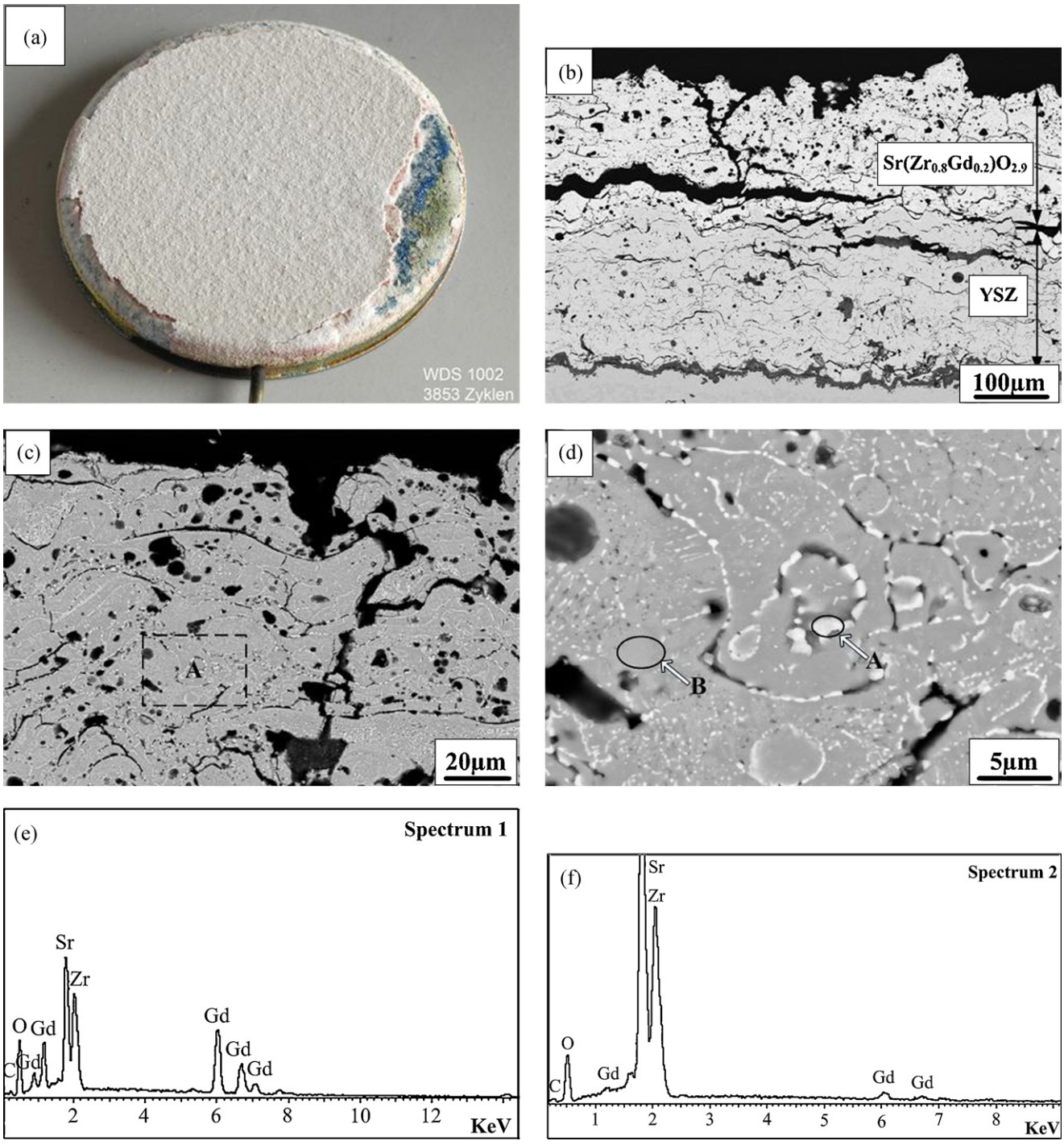

Fig. 8. Surface morphology of $Sr(Zr_{0.8}Gd_{0.2})O_{2.9}$/YSZ DLC (a), its cross-section micrographs (b), (c) and (d) (high magnification of area A in (c)), EDX spectra of areas A (e) and B (f) in (d), after cycling at a surface temperature of 1249 °C.

not only at the bondcoat–YSZ interface, but also at the YSZ–$Sr(Zr_{0.8}Gd_{0.2})O_{2.9}$ interface, whereas the vertical cracks are observed only in the $Sr(Zr_{0.8}Gd_{0.2})O_{2.9}$ layer (Fig. 8(b)). In the $Sr(Zr_{0.8}Gd_{0.2})O_{2.9}$ layer (Fig. 8(d)), the area A is rich in the Gd element compared to area B as shown by EDX analysis, indicating that Gd precipitated upon cycling. According to the XRD results the precipitated particles are Gd_2O_3. The failure mechanism of the $Sr(Zr_{0.8}Gd_{0.2})O_{2.9}$/YSZ coating is mainly due to the TGO growth, but the failure of the coating seems to be enhanced by crack development in the $Sr(Zr_{0.8}Gd_{0.2})O_{2.9}$ layer. The crack development in the $Sr(Zr_{0.8}Gd_{0.2})O_{2.9}$ layer might be attributed to its lower TEC compared to $Sr(Zr_{0.9}Yb_{0.1})O_{2.95}$, and the lower TEC is clearly seen in Fig. 1.

The morphology of $Sr(Zr_{0.8}Gd_{0.2})O_{2.9}$/YSZ coating surface and its cross-section after cycling at a surface temperature of 1348 °C are shown in Fig. 9. It is clear in Fig. 9(a) that sintering of the coating surface occurred, and that the surface spalled from the $Sr(Zr_{0.8}Gd_{0.2})O_{2.9}$ layer. This is confirmed by XRD

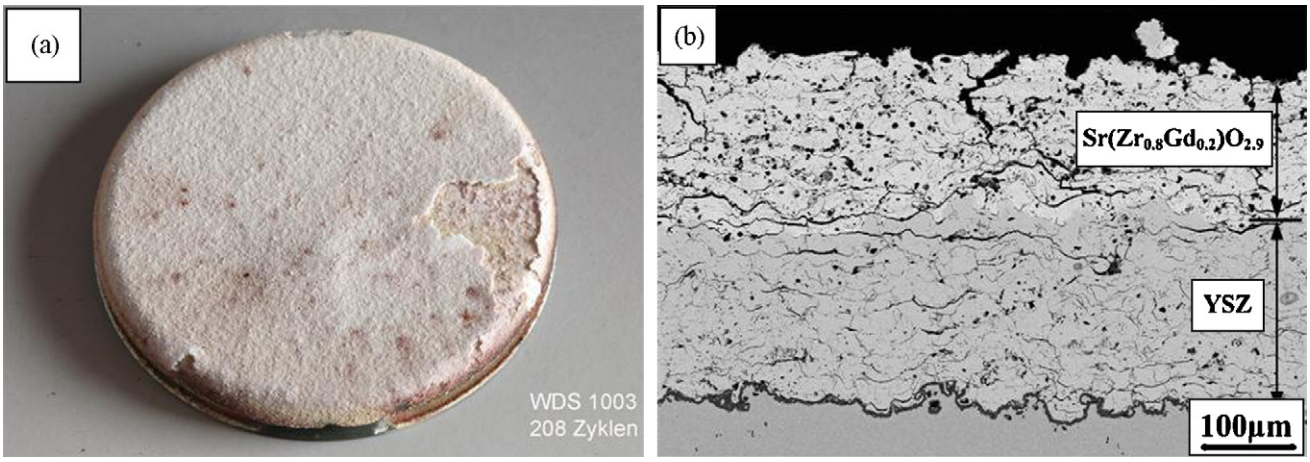

Fig. 9. Surface morphology of $Sr(Zr_{0.8}Gd_{0.2})O_{2.9}$/YSZ DLC (a) and its cross-section micrograph (b) after cycling at a surface temperature of 1348 °C.

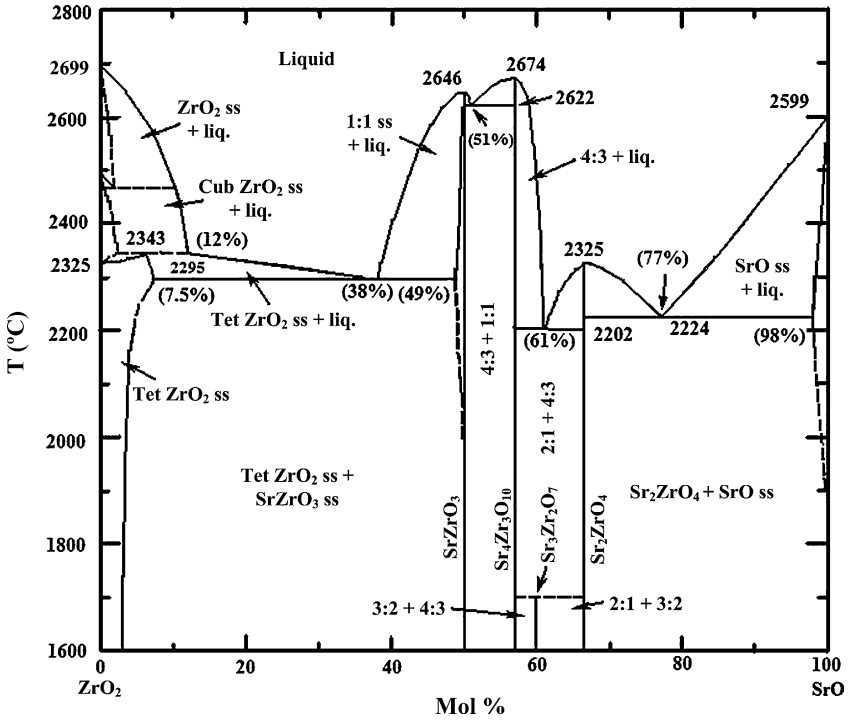

Fig. 10. ZrO_2–SrO phase diagram.[42]

analysis, because there is no YSZ diffraction peak after thermal cycling.

The precipitation of Yb_2O_3 and Gd_2O_3 in the $Sr(Zr_{0.9}Yb_{0.1})O_{2.95}$ and $Sr(Zr_{0.8}Gd_{0.2})O_{2.9}$ coatings upon cycling can be explained as follows. It is believed to be due to the different vapor pressures for ZrO_2, SrO, Yb_2O_3 and Gd_2O_3, which are 1×10^{-6} atm (2500 °C), 2×10^{-5} atm (2500 °C), 6×10^{-8} atm (2500 °C) and 9×10^{-6} atm (2500 °C), respectively.[40,41] The ZrO_2–SrO phase diagram[42] is shown in Fig. 10. During thermal spraying SrO volatilizes more than ZrO_2 due to its higher vapor pressure, resulting in the coating composition deviating from stoichiometric $SrZrO_3$. Zr is partially substituted in $SrZrO_3$ by Yb or Gd, and the vapor pressure of SrO is higher than that of both Yb_2O_3 and Gd_2O_3. Therefore the mixture of $SrZrO_3$ and the small amount of Yb_2O_3 or Gd_2O_3 mean that the non-equilibrium Yb_2O_3 or Gd_2O_3 in the as-sprayed coatings transforms into equilibrium phase upon cycling. The amount of Yb_2O_3 or Gd_2O_3 in the coatings increases upon cycling, which might be due to their limited solubility in $SrZrO_3$ at lower temperatures compared to the synthesis temperature of $Sr(Zr_{0.9}Yb_{0.1})O_{2.95}$ and $Sr(Zr_{0.8}Gd_{0.2})O_{2.9}$.

5. Conclusions

$Sr(Zr_{0.9}Yb_{0.1})O_{2.95}$ and $Sr(Zr_{0.8}Gd_{0.2})O_{2.9}$ were investigated for their potential as TBC materials. The TEC of $Sr(Zr_{0.9}Yb_{0.1})O_{2.95}$ is $9.2–10.6 \times 10^{-6}\,K^{-1}$ (200–1100 °C), which is comparable to that of YSZ. A lower TEC for $Sr(Zr_{0.8}Gd_{0.2})O_{2.9}$ is a disadvantage for TBC application. The

results of specific heat capacity and thermal conductivity measurements reveal that doping Yb_2O_3 is more effective in reducing the specific heat capacity and thermal conductivity for $SrZrO_3$ than doping Gd_2O_3. The thermal conductivity of $Sr(Zr_{0.9}Yb_{0.1})O_{2.95}$ is ~20% lower than that of $SrZrO_3$ in the whole tested temperature range, which is beneficial for thermal insulation. The Young's moduli of these two materials were found to be lower than that of YSZ, which might yield higher strain tolerance for coatings. A fracture toughness of 1.1 MPa $m^{1/2}$ for $Sr(Zr_{0.9}Yb_{0.1})O_{2.95}$ and 1.6 MPa $m^{1/2}$ for $Sr(Zr_{0.8}Gd_{0.2})O_{2.9}$ was comparable to that of plasma-sprayed YSZ coatings.

Furthermore, compared to short thermal cycling lifetime for $Sr(Zr_{0.9}Yb_{0.1})O_{2.95}$ and $Sr(Zr_{0.8}Gd_{0.2})O_{2.9}$ coatings, the $Sr(Zr_{0.9}Yb_{0.1})O_{2.95}$/YSZ and $Sr(Zr_{0.8}Gd_{0.2})O_{2.9}$/YSZ DLC had much longer thermal cycling lifetimes at a surface temperature of ~1250 °C, which is comparable to that of YSZ coating at a similar surface temperature. A major advantage of $Sr(Zr_{0.9}Yb_{0.1})O_{2.95}$/YSZ DLC is that its thermal cycling lifetime was ~25% longer than that of the optimized YSZ coating at a surface temperature of ~1350 °C, which indicates that $Sr(Zr_{0.9}Yb_{0.1})O_{2.95}$ is a promising material for TBC applications at higher temperatures than possible with YSZ. A short thermal cycling lifetime of $Sr(Zr_{0.8}Gd_{0.2})O_{2.9}$/YSZ DLC at a surface temperature of ~1350 °C is believed to be due to the relatively lower TEC and higher sintering rate for $Sr(Zr_{0.8}Gd_{0.2})O_{2.9}$.

Acknowledgements

The authors would like to thank Mr. F. Vondahlen, Mrs. M. Andreas and Mrs. N. Adels (all IEF1, FZJ) for preparing and testing the samples, Mr. F. Tietz and Mrs. A. Hilgers (both IEF1, FZJ) and Mr. D. Pitzer (BNM, FZJ) for measurements of the samples' thermophysical properties, Mrs. S. Schwartz-Lückge for the porosity measurements and Mr. M. Kappertz (both IEF1, FZJ) for preparing the cross-sections, Mr. W. Fischer (IEF1, FZJ) for XRD measurements.

References

1. Miller, R. A., Thermal barrier coatings for aircraft engines: history and directions. *J. Therm. Spray Technol.*, 1997, **6**(1), 35–42.
2. Nelson, W. A. and Orenstein, R. M., TBC experience in land-based gas turbines. *J. Therm. Spray Technol.*, 1997, **6**(2), 176–180.
3. Miller, R. A., Smialek, J. L. and Garlick, R. G., Phase stability in plasma-sprayed partially stabilized Zirconia-Yttria, in Advances in Ceramics, Vol. 3, *Science and Technology of Zirconia*. In A. H. Heuer and L. W. Hobbs, ed., American Ceramic Society, Columbus, OH, 1981, pp. 241–251.
4. Clarke, D. R. and Phillpot, S. R., Thermal barrier coating materials. *Mater. Today*, 2005, **8**(6), 22–29.
5. Zhu, D. and Miller, R. A., Thermal conductivity and sintering behavior of advanced thermal barrier coatings. NASA Report TM-2002-211481, NASA, Cleveland, 2002.
6. Zhu, D. and Miller, R. A., Hafnia-based materials developed for advanced thermal environmental barrier coating applications. NASA Report TM-2005-192261, NASA, Cleveland, 2004.
7. Ma, W., Gong, S., Xu, H. and Cao, X., The thermal cycling behavior of lanthanum-cerium oxide thermal barrier coating prepared by EB-PVD. *Surf. Coat. Technol.*, 2006, **200**, 5113–5118.
8. Cao, X., Vassen, R., Fischer, W., Tietz, F., Jungen, W. and Stöver, D., Lanthanum-cerium oxide as a thermal barrier-coating material for high-temperature applications. *Adv. Mater.*, 2003, **15**(17), 1438–1442.
9. Suresh, G., Seenivasan, G., Krishnaiah, M. V. and Murti, P. S., Investigation of the thermal conductivity of selected compounds of lanthanum, samarium and europium. *J. Alloy Compd.*, 1998, **269**(1–2), L9–L12.
10. Lehmann, H., Pitzer, D., Pracht, G., Vassen, R. and Stöver, D., Thermal conductivity and thermal expansion coefficients of the lanthanum rare-earth-element zirconate system. *J. Am. Ceram. Soc.*, 2003, **86**(8), 1338–1344.
11. Stöver, D., Pracht, G., Lehmann, H., Dietrich, M., Döring, J. and Vassen, R., New material concepts for the next generation of plasma-sprayed thermal barrier coatings. *J. Therm. Spray Technol.*, 2003, **13**(1), 76–83.
12. Vassen, R., Traeger, F. and Stöver, D., New thermal barrier coatings based on pyrochlore/YSZ double-layer systems. *Int. J. Appl. Ceram. Technol.*, 2004, **1**(4), 351–361.
13. Padture, N. P. and Klemens, P. G., Low thermal conductivity in garnets. *J. Am. Ceram. Soc.*, 1997, **80**(4), 1018–1020.
14. Sudre, O., Cheung, J., Marshall, D., Morgan, P. and Levi, C. G., Thermal insulation coatings of $LaPO_4$. In *The 25th Annual International Conference on Composites, Advance Ceramics, Materials, and Structures: B*, ed. M. Singh and T. Jessen, 2001, pp. 367–374.
15. Gadow, R. and Lischka, M., Lanthanum hexaaluminate – novel thermal barrier coatings for gas turbine applications – materials and process development. *Surf. Coat. Technol.*, 2002, **151–152**, 392–399.
16. Heimberg, B., Beele, W., Kempter, K., Bast, U., Haubold, T., Hoffmann, M., Endriss, A., Greil, P., Hong, C., Aldinger, F. and Seifert, H., Process for production of a ceramic thermal barrier layer for gas turbine engine component. *US patent 6602553 B2*, 2003.
17. Vassen, R., Cao, X., Tietz, F., Basu, D. and Stöver, D., Zirconates as new materials for thermal barrier coatings. *J. Am. Ceram. Soc.*, 2000, **83**(8), 2023–2028.
18. Howard, C. J. and Stokes, H. T., Structures and phase transitions in perovskites—a group-theoretical approach. *Acta Cryst.*, 2005, **A61**, 93–111.
19. Carlsson, L., High-temperature phase transitions in $SrZrO_3$. *Acta Cryst.*, 1967, **23**, 901–905.
20. Ahtee, A., Ahtee, M., Glazer, A. M. and Hewat, A. W., The structure of orthorhombic $SrZrO_3$ by neutron powder diffraction. *Acta Cryst.*, 1976, **B32**, 3243–3246.
21. Ahtee, M., Glazer, A. M. and Hewat, A. W., High-temperature phases of $SrZrO_3$. *Acta Cryst.*, 1978, **B34**, 752–758.
22. Howard, C. J., Knight, K. S., Kennedy, B. J. and Kisi, E. H., The structural phase transitions in strontium zirconate revisited. *J. Phys.: Condens. Matter*, 2000, **12**, L677–L683.
23. Zhao, Y. and Weidner, D. J., Thermal expansion of $SrZrO_3$ and $BaZrO_3$ perovskites. *Phys. Chem. Miner.*, 1991, **18**, 294–301.
24. Ligny, D. and Richet, P., High-temperature heat capacity and thermal expansion of $SrTiO_3$ and $SrZrO_3$ perovskites. *Phys. Rev. B*, 1996, **53**(6), 3013–3022.
25. Nicholls, J. R., Lawson, K. J., Johnstone, A. and Rickerby, D. S., Method to reduce the thermal conductivity of EB-PVD TBCs. *Surf. Coat. Technol.*, 2002, **151–152**, 383–391.
26. Kingery, W. D., Bowen, H. K. and Uhlmann, D. R., *Introduction to ceramics* (*2nd ed.*). Wiley-Interscience, New York, 1976.
27. Stack, G. A., The thermal conductivity of non-metallic crystals. *Solid State Phys.*, 1979, **34**, 1–71.
28. Clarke, D. R., Materials selection guidelines for low thermal conductivity thermal barrier coatings. *Surf. Coat. Technol.*, 2003, **163–164**, 67–74.
29. Klemens, P. G., Theory of the thermal conductivity of solids. In *Thermal conductivity*, *Vol. 1*, ed. R. P. Tye. Academic Press, London and New York, 1969, pp. 2–65.
30. Soyez, G., Eastman, J. A., Thompson, L. J., Bai, G., Baldo, P. M., McCormick, A. W., DiMelfi, R. J., Elmustafa, A. A., Tambwe, M. F. and Stone, D. S., Grain-size-dependent thermal conductivity of nanocrystalline yttria-stabilized zirconia films grown by metal-organic chemical vapor deposition. *Appl. Phys. Lett.*, 2000, **77**(8), 1155–1157.
31. Li, C., Soh, K. and Wu, P., Formability of ABO_3 perovskites. *J. Alloys Compd.*, 2004, **372**, 40–48.

32. Roher, G. S., *Structure and bonding in crystalline materials*. Cambridge University Press, New York, 2001.
33. Shannon, R. D., Revised effective ionic radii and systematic studies of interatomic distances in halides and chalcogenides. *Acta Cryst.*, 1976, **A32**, 751–767.
34. Traeger, F., Ahrens, M., Vassen, R. and Stöver, D., A life time model for ceramic thermal barrier coatings. *Mater. Sci. Eng.*, 2003, **A358**, 255–265.
35. Morrell, R., *Handbook of properties of technical and engineering ceramics, Part 1*. Her Majesty's Stationery Office, London, U.K., 1989.
36. Vassen, R., Tietz, F., Kerkhoff, G., Wilkenhöner, R. and Stöver, D., New materials for advanced thermal barrier coatings. In *Proceedings of the 6th Liège Conference, Part III, Materials for Advanced Power Engineering*, ed. J. Lecomte-Beckers, F. Schubert and P. J. Ennis. Forschungszentrum Jülich GmbH, Jülich, Germany, 1998, pp. 1627–1635.
37. Stecura, S., Optimization of the Ni–Cr–Al–Y/ZrO_2–Y_2O_3 thermal barrier system. *Adv. Ceram. Mater.*, 1986, **1**(1), 68–76.
38. Bast, U. and Schumann, E., Development of novel oxide materials for TBCs. *Ceram. Eng. Sci. Proc.*, 2002, **23**, 525–532.
39. Vassen, R., Kerkhoff, G. and Stöver, D., Development of a micromechanical life prediction model for plasma sprayed thermal barrier coatings. *Mater. Sci. Eng.*, 2001, **A303**(1–2), 100–109.
40. Jacobson, N., Thermodynamic properties of some metal oxide–zirconia systems. *NASA TM*, 1989, **102351**.
41. Schulz, U., Saruhan, B., Fritscher, K. and Leyens, C., Review on advanced EB-PVD ceramic topcoats for TBC applications. *Int. J. Appl. Ceram. Technol.*, 2004, **1**(4), 302–315.
42. Noguchi, T., Okubo, T. and Yonemochi, O., Reactions in the system ZrO_2–SrO. *J. Am. Ceram. Soc.*, 1969, **52**(4), 178–181.